



Cross Talking Calcium, IP₃ and Buffer Dynamics Alters ATP and NADH Level in Obese and Normal Hepatocyte Cell

Vedika Mishra¹ · Neeru Adlakha¹

Accepted: 8 May 2024 / Published online: 24 May 2024

© The Author(s), under exclusive licence to Springer Science+Business Media, LLC, part of Springer Nature 2024

Abstract

The cross talk between calcium (Ca²⁺), IP₃ and buffer dynamics regulate various mechanisms in hepatocyte cells. The study of independent systems of calcium, IP₃, and buffer signaling provides limited information about cell dynamics. In the current study, coupled reaction-diffusion equations are used to design a cross-talk model for IP₃, buffer, and calcium dynamics in a hepatocyte cell. The one-way feedback of calcium, buffer, and IP₃ in ATP production, ATP degradation, and NADH production rate is incorporated into the model. Numerical simulation has been done using the Finite Element Method (FEM) along the spatial direction and the Crank-Nicolson (C-N) method along the temporal direction. The numerical results are analysed to determine the effects of alterations in processes of cross-talking dynamics of IP₃, buffer, and calcium on ATP and NADH production and degradation rate of ATP in a hepatocyte cell under normal and obesity conditions. The comparative analysis of these findings unveils notable distinctions induced by obesity in calcium dynamics, ATP and NADH synthesis, and ATP degradation kinetics.

Keywords Finite Element Method · Reaction diffusion equation · Calcium · IP₃ · Buffer

Introduction

Metabolism, detoxification, and homeostasis regulation in the body are mainly controlled by the liver. The parenchyma of the liver is arranged into lobules, which are hexagonal in shape, each consisting of a central vein surrounded by a portal triad. Each portal triad consists of a hepatic vein, bile duct, and hepatic artery. The hepatocytes are the predominant cells, comprising 70% of the liver. In the liver, cholangiocytes, endothelial, stellate, kupffer, and oval cells are the non-parenchymal cells. These cells perform many important functions in the liver [1].

Various activities of the cells have been regulated using Ca²⁺ which acts as an intracellular messenger in the cells. Through two different types of channels, Ca²⁺ is released from the intracellular stores (endoplasmic reticulum (ER)) in the cytosol. One of these is the family of inositol 1,4,5-triphosphate receptors (IP3R). IP₃ is produced by receptor activation of phosphoinositide-specific phospholipase C

(PLC), causing the activation of IP3Rs [2]. Ryanodine receptors (RyR) which are the second family of intracellular Ca²⁺ channels, were named due to their great affinity for the plant alkaloid ryanodine [2]. Hepatocyte's canalicular region contains a majority of the type II IP3R, while other cytosolic regions include more of the type I IP3R and less of the type II receptor [3].

Many researchers have investigated calcium signaling in diverse cell types such as neurons, myocytes, oocytes, pancreatic acinar cells, fibroblasts, astrocytes, and hepatocytes, among others [4–11].

Kotwani et al. [7, 12, 13]; Hemant et al. [14, 15]; Naik et al. [8, 16–22]; Pathak et al. [10, 23] and Jha et al. [24, 25] studied calcium distribution involving various parameters such as excess buffer, RyR, voltage-gated calcium channels, etc. for fibroblasts, lymphocytes, oocytes, myocytes, and astrocytes, respectively. Panday et al. [9, 26] devised a model for Ca²⁺ dynamics in oocytes that took into account Ca²⁺ advection within the cell. Amrita et al. [4, 5, 27] employed a finite element method to investigate how source geometry, NCX, SERCA pump, leak, and other factors influence Ca²⁺ distributions in neuron cells and dendritic spines. Manhas et al. [28, 29] reported the impact of mitochondria on Ca²⁺ signaling while studying calcium fluctuation in pancreatic acinar cells. Tewari et al. [11, 30]

✉ Vedika Mishra
vedikamishra1996@gmail.com

¹ Department of Mathematics, SVNIT, Surat 395007 Gujarat, India

and Jagtap et al. [6, 31, 32] studied calcium dynamics in neurons and hepatocytes, respectively. Vedika et al. [33, 34] studied Ca^{2+} dynamics in obese and normal hepatocyte cells. The interdependent effect of calcium and buffer dynamics was also examined. Kothiya et al. [35–38] studied the system dynamics of calcium in a fibroblast cell. Vaishali et al. [39, 40] studied calcium dynamics in pancreatic β cells.

Hajnoczky et al. [41] discussed that the predominant elevation of calcium concentration ($[Ca^{2+}]$) in non-excitable cells is via the second messenger IP_3 . Politi et al. [42] formulated a model aimed at explaining the calcium-triggered stimulation of phospholipase C and IP_3 3-kinase. This model captures the mechanisms through which calcium orchestrates both the enhancing and diminishing influences on IP_3 metabolism. Jean et al. [43] found that the liver's IP_3R was co-purified with markers of the plasma membrane. Thurley et al. [44] discovered that a stochastic calcium spike is produced by the interaction of IP_3R clusters. Wagner et al. [45] modeled fertilization of a xenopus egg's Ca^{2+} wave in one dimension using cartesian coordinates. Handy et al. [46] did the bifurcation simulations and analysis for the study of IP_3 dependent calcium variation. To investigate nonlinear IP_3 dependent calcium dynamics in cardiac myocytes, Singh et al. [47] devised a mathematical model for myocytes. Pawar et al. [48–53] studied the interdependence of Ca^{2+} on IP_3 , NO, dopamine, β -amyloid etc. for neuron cells using mathematical models. Pawar et al. [54, 55] have also discussed calcium and the system dynamics of calcium with other ions using a fractional reaction-diffusion equation.

Neher et al. [56] investigated the calcium gradient and buffer in chromaffin cells derived from cows and concluded that out of total Ca^{2+} that enters the cell, 98–99% Ca^{2+} bind with endogenous Ca^{2+} buffer. Smith et al. [57–60] considered the three-parameter regimes given by the rate of response and dimensionless diffusion coefficients of Ca^{2+} and buffer with regard to each other. Martin Falcke [61] found that the concentration profile of a fast buffer around an open channel is more localized than that of a slow buffer. Through, the construction of a mathematical model, M.D. Stern [62] showed that the stabilization of rapid fluctuations in Ca^{2+} fluxes requires a buffer with rapid kinetics. According to Prins et al. [63], one thing that all organellar Ca^{2+} buffers have in common is their multifunctionality, as evidenced by the variety of Ca^{2+} binding and reactions they display. In addition to serving as an inactive Ca^{2+} breakdown within intracellular organelles, Ca^{2+} buffering proteins also modulate the Ca^{2+} release pathway, fold proteins, and regulate apoptosis. Gabso et al. [64, 65] highlighted the significant role of cellular calcium buffers in modulating the intensity and diffusion of calcium signals within neurons.

The literature review suggests a notable gap in research concerning the complex interplay of calcium, IP_3 , and buffering dynamics within hepatocyte cells. Previous studies have predominantly modeled buffering dynamics as static, failing to account for their dynamic nature. This oversight simplifies the intricate relationships between calcium dynamics and other cellular processes, such as the interaction of calcium with IP_3 , nitric oxide (NO), and dopamine, where buffers were assumed to be constant. However, recognizing that buffer concentrations are indeed variable can lead to more accurate and insightful models. The effects of changes in the mechanisms governing independent Ca^{2+} dynamics on the synthesis and degradation of ATP as well as the synthesis of NADH in normal and obese hepatocyte cells have received very little attention in previous studies. But no attempt is reported in the literature for the study of the effects of changes in the mechanisms governing cooperative Ca^{2+} , IP_3 , and buffer dynamics on the synthesis and degradation of ATP as well as the synthesis of NADH in normal and obese hepatocyte cells. Thus, a new model is developed in this paper to explore better insights into biophysical mechanisms and their effects on calcium, buffer, and IP_3 dynamics, as well as their consequential impacts on the synthesis and degradation of ATP as well as the synthesis of NADH in normal and obese hepatocyte cells. The model integrates the coupled reaction-diffusion equations for Ca^{2+} , IP_3 and buffers through their mutual fluxes, aims to provide a deeper understanding of these processes. Numerical simulations were conducted using the FEM combined with the C-N Method to explore these dynamics further.

Problem Formulation

The reaction-diffusion equation proposed by Wagner et al. [45] is modified by incorporating calcium buffering fluxes and reaction term for Ca^{2+} profile in one dimensional unsteady state case which is expressed as:

$$\frac{\partial[Ca^{2+}]}{\partial t} = D_{Ca} \frac{\partial^2[Ca^{2+}]}{\partial x^2} + \frac{[J_{IP3R} + J_{LK} - J_{SERCA}]}{V_c} - J_{on} + J_{off}. \quad (1)$$

Here, $[Ca^{2+}]$ represents calcium concentration in the cytosol, D_{Ca} represents diffusion coefficient of calcium in hepatocyte cell, J_{IP3R} is flux due to IP_3 receptor, J_{LK} denotes leak from ER, J_{SERCA} is efflux from cytosol to ER, J_{on} and J_{off} represent Ca^{2+} buffering fluxes.

The different fluxes are modeled as,

$$J_{IP3R} = V_{IP3R} m^3 h^3 ([Ca^{2+}]_{ER} - [Ca^{2+}]), \quad (2)$$

Where, V_{IP3R} is IP_3 receptor flux rate constant, $[Ca^{2+}]_{ER}$ is calcium concentration in ER [45].

$$m = \frac{V}{K_{IP3R} + V} \frac{[Ca^{2+}]}{[Ca^{2+}] + K_{Act}}, \tag{3}$$

Here, V represents IP_3 concentration in the cytosol [45]. The proportion of subunits that Ca^{2+} has not yet inactivated is represented by the variable h ,

$$\frac{dh}{dt} = \frac{h_{\infty} - h}{\tau}, \tag{4}$$

Here,

$$h_{\infty} = \frac{K_{Inh}}{K_{Inh} + [Ca^{2+}]}, \tag{5}$$

$$J_{LK} = V_{Leak}([Ca^{2+}]_{ER} - [Ca^{2+}]), \tag{6}$$

Here, V_{Leak} is rate of ER leakage.

$$J_{SERCA} = V_{SERCA} \frac{[Ca^{2+}]^2}{K_{SERCA}^2 + [Ca^{2+}]^2}, \tag{7}$$

Here, SERCA's half-maximal activating cytosolic Ca^{2+} concentration is K_{SERCA} and its maximum outflow from the bulk cytosol is V_{SERCA} .

$$J_{on} = k_j^+ [Ca^{2+}]b, \tag{8}$$

$$J_{off} = k_j^- \frac{b_{tot}[Ca^{2+}]}{K + [Ca^{2+}]}, \tag{9}$$

Here, association and dissociation rate of buffer are represented by k_j^+ and k_j^- respectively [57, 66].

The following provides cytosolic IP_3 concentration(V)'s reaction-diffusion equation [45],

$$\frac{\partial V}{\partial t} = D_I \frac{\partial^2 V}{\partial x^2} + \frac{J_{Production} - \lambda(J_{Kinase} + J_{Phosphatase})}{V_c}. \tag{10}$$

Here, the diffusion coefficient of IP_3 is D_I , production of IP_3 due to Ca^{2+} is $J_{Production}$, J_{Kinase} and $J_{Phosphatase}$ are IP_3 degradation due to 3-kinase and 5-phosphatase given as [45],

$$J_{Production} = V_{Production} \frac{[Ca^{2+}]^2}{[Ca^{2+}]^2 + K_{Production}^2}, \tag{11}$$

$$J_{Kinase} = (1 - \theta)V_1 \frac{V}{V + 2.5} + \theta V_2 \frac{V}{V + 0.5}, \tag{12}$$

$$J_{Phosphatase} = V_3 \frac{V}{V + 30}, \tag{13}$$

Here, θ is given by,

$$\theta = \frac{[Ca^{2+}]}{[Ca^{2+}] + 0.39}, \tag{14}$$

The nullcline-a surface along which the variable does not change is obtained by solving for the variable while setting each reaction-diffusion equation's right side to zero. The result of h nullcline is $h=h_{\infty}$. Therefore, it gives,

$$h = \frac{K_{Inh}}{K_{Inh} + [Ca^{2+}]}, \tag{15}$$

The buffer(b) dynamics has been modeled using the following diffusion equation [66],

$$\frac{\partial b}{\partial t} = D_b \frac{\partial^2 b}{\partial x^2} - J_{on} + J_{off}. \tag{16}$$

Where, J_{on} and J_{off} are given in equations (8) and (9)

Based on the presumption that the Ca^{2+} , buffer and IP_3 concentrations in cell are 0.1, 0 and 0.16 μM respectively, at rest, the following initial conditions are imposed [6].

$$([Ca^{2+}]_{t=0}) = 0.1 \mu M, \tag{17}$$

$$V_{t=0} = 0.16 \mu M, \tag{18}$$

$$(b_{t=0}) = 0 \mu M, \tag{19}$$

To arrive at the solution, the following boundary conditions are used [6].

$$\lim_{x \rightarrow 0} \left(-D_{Ca} \left(\frac{\partial [Ca^{2+}]}{\partial x} \right) \right) = \sigma_{Ca}, \tag{20}$$

Where, σ_{Ca} represents source influx.

$$\lim_{x \rightarrow 15} ([Ca^{2+}]) = C_{\infty} = 0.1 \mu M, \tag{21}$$

$$\lim_{x \rightarrow 15} (V) = 0.16 \mu M, \tag{22}$$

$$\lim_{x \rightarrow 0} (V) = V_{\infty} = 3 \mu M, \tag{23}$$

$$\lim_{x \rightarrow 0} D_b \left(\frac{\partial b}{\partial x} \right) = 0, \tag{24}$$

$$\lim_{x \rightarrow 15} (b) = b_{\infty} = \frac{Kb_{tot}}{K + C_{\infty}}, \tag{25}$$

Here, total buffer concentration is b_{tot} and $K = \frac{k^-}{k^+}$ is buffer's dissociation constant [32, 34].

ATP degradation rate-calcium dependent is calculated using [67],

$$J_{HYD} = \frac{J_{SERCA}}{2} + K_{HYD} \frac{[ATP]_c}{[ATP]_c + K_h}. \tag{26}$$

J_{SERCA} is calculated using Eq. (7).

For ATP hydrolysis, the Michaelis-Menten constant is K_h and the maximal rate is K_{HYD} and cytosolic ATP concentration is $[ATP]_c$.

Ca^{2+} -dependent ATP production is computed by [68],

$$ATP(C) = \frac{\frac{F_o}{F_o-1} - 2 \frac{[Ca^{2+}]}{[Ca^{2+}]_{max}}}{\frac{1}{F_o-1} - \left(\frac{[Ca^{2+}]}{[Ca^{2+}]_{max}}\right)^2}. \tag{27}$$

IP_3 -dependent ATP production is computed by [68],

$$ATP(V) = \frac{\frac{G_o}{G_o-1} - 2 \frac{V}{V_{max}}}{\frac{1}{G_o-1} - \left(\frac{V}{V_{max}}\right)^2}. \tag{28}$$

NADH production rate is calculated by [67],

$$I_{AGC} = V_{AGC} \frac{[Ca^{2+}]}{K_{AGC} + [Ca^{2+}]} \frac{q_2}{q_2 + c_m} \exp(p_4 V_m). \tag{29}$$

Where, K_{AGC} and V_{AGC} , respectively, represent the rate constants for the synthesis of NADH and calcium’s dissociation from the aspartate-glutamate carrier (AGC).

The Taylor’s approximation method is used to linearize the proposed problem approximately where the IP_3 concentration is $3 \mu M$, buffer concentration is $5 \mu M$ and $[Ca^{2+}]$ is $0.1 \mu M$. Since the Ca^{2+} , buffer and IP_3 concentrations are constrained to a restricted range, the nonlinear parts of the Taylor’s series become insignificant.

After linearisation, Eq. (1) can be rewritten as follows:

$$\frac{\partial u}{\partial t} = D_{Ca} \frac{\partial^2 u}{\partial x^2} + A_1 u + B_1 V + C_1 b + D_1, \tag{30}$$

The constants A_1, B_1, C_1 and D_1 were found using Taylor’s approximation approach (TAA) and u stands for $[Ca^{2+}]$.

Equation (10) can be redefined as, in a similar way for IP_3 concentration as V .

$$\frac{\partial V}{\partial t} = D_I \frac{\partial^2 V}{\partial x^2} + A_2 u + B_2 V + C_2 b + D_2, \tag{31}$$

The constants A_2, B_2, C_2 and D_2 were found using TAA.

It is possible to rewrite Eq. (16) as,

$$\frac{\partial b}{\partial t} = D_b \frac{\partial^2 b}{\partial x^2} + A_3 u + B_3 V + C_3 b + D_3, \tag{32}$$

Where A_3, B_3, C_3 and D_3 were found using TAA.

The numerical results are derived employing the variational finite element methodology applied to the

cytoplasmic domain of the hepatocyte cell, segmented into 80 linear elements. The discretized variational functional of Eq. (30) is depicted as follows:

$$J^{(e)} = \frac{1}{2} \int_{x_m}^{x_n} \left[u^{(e)2} + \frac{1}{D_{Ca}} \frac{\partial u^{(e)2}}{\partial t} - A_1 u^{(e)2} - 2B_1 V^{(e)} u^{(e)} - 2C_1 b^{(e)} u^{(e)} - 2D_1 u^{(e)} \right] dx - \mu^{(e)} \left(\frac{\partial u^{(e)}}{\partial x} u^{(e)} \right)_{(x=0)}, \tag{33}$$

$\mu^{(e)}$ is equal to 1 for the first element and 0 for every further element.

The shape function for calcium concentration is given as the following linear fluctuation due to the small size of the elements.

$$u^{(e)} = c_1 + c_2 x, \tag{34}$$

The Eq. (34) can be expressed as

$$u^{(e)} = Q^T C^{(e)}, \tag{35}$$

Here,

$$Q^T = [1 \quad x] \ \& \ C^{(e)} = \begin{bmatrix} c_1 \\ c_2 \end{bmatrix}$$

Values of $u^{(e)}$ at nodes x_m and x_n are given by,

$$u^{(e)}(x_m) = c_1 + c_2 x_m, \tag{36}$$

$$u^{(e)}(x_n) = c_1 + c_2 x_n, \tag{37}$$

Using above equations, it is obtained as,

$$\bar{u}^{(e)} = Q^{(e)} C^{(e)}, \tag{38}$$

Here, $Q^{(e)} = \begin{bmatrix} 1 & x_m \\ 1 & x_n \end{bmatrix}$ & $\bar{u}^{(e)} = \begin{bmatrix} u_m \\ u_n \end{bmatrix}$

From Eqs. (36)–(38) we obtain,

$$u^{(e)} = Q^T S^{(e)} \bar{u}^{(e)}, \tag{39}$$

Here, $S^{(e)} = Q^{(e)-1} = \frac{1}{x_n - x_m} \begin{bmatrix} x_n & -x_m \\ -1 & 1 \end{bmatrix}$

$$J^{(e)} = J_k^{(e)} + J_m^{(e)} - J_l^{(e)} - J_r^{(e)} - J_p^{(e)} - J_q^{(e)} - J_s^{(e)}, \tag{40}$$

Where,

$$J_k^{(e)} = \frac{1}{2} \int_{x_m}^{x_n} \left[\left(Q_x^T S^{(e)} \bar{u}^{(e)2} \right) \right] dx, \tag{41}$$

$$J_m^{(e)} = \frac{1}{2} \int_{x_m}^{x_n} \frac{1}{D_{Ca}} \frac{\partial}{\partial t} \left[\left(Q^T S^{(e)} \bar{u}^{(e)2} \right) \right] dx, \tag{42}$$

$$J_l^{(e)} = \frac{1}{2} \int_{x_m}^{x_n} A_1 \left[\left(Q^T S^{(e)} \bar{u}^{(e)} \right)^2 \right] dx, \tag{43}$$

$$J_r^{(e)} = \int_{x_m}^{x_n} B_1 \left[\left(Q^T S^{(e)} \bar{u}^{(e)} Q^T S^{(e)} \bar{v}^{(e)} \right) \right] dx, \tag{44}$$

$$J_p^{(e)} = \int_{x_m}^{x_n} C_1 \left[\left(Q^T S^{(e)} \bar{u}^{(e)} Q^T S^{(e)} \bar{b}^{(e)} \right) \right] dx, \tag{45}$$

$$J_q^{(e)} = \int_{x_m}^{x_n} D_1 \left[\left(Q^T S^{(e)} \bar{u}^{(e)} \right) \right] dx, \tag{46}$$

$$J_s^{(e)} = \mu^{(e)} \left[\left(\frac{\sigma_{Ca}}{2D_{Ca}} Q^T S^{(e)} \bar{u}_{(x=0)}^{(e)} \right) \right], \tag{47}$$

Minimizing $J^{(e)}$ with respect to $\bar{u}^{(e)}$,

$$\frac{dJ^{(e)}}{d\bar{u}^{(e)}} = 0, \tag{48}$$

That is,

$$\frac{dJ^{(e)}}{d\bar{u}^{(e)}} = \frac{dJ_k^{(e)}}{d\bar{u}^{(e)}} + \frac{dJ_m^{(e)}}{d\bar{u}^{(e)}} - \frac{dJ_l^{(e)}}{d\bar{u}^{(e)}} - \frac{dJ_r^{(e)}}{d\bar{u}^{(e)}} - \frac{dJ_p^{(e)}}{d\bar{u}^{(e)}} - \frac{dJ_q^{(e)}}{d\bar{u}^{(e)}} - \frac{dJ_s^{(e)}}{d\bar{u}^{(e)}}, \tag{49}$$

Which can be written as,

$$\frac{dJ}{d\bar{u}^{(e)}} = \sum_{e=1}^{80} \bar{M}^{(e)} \frac{dJ^{(e)}}{d\bar{u}^{(e)}} \left(\bar{M}^{(e)} \right)^T = 0, \tag{50}$$

Where,

$$\bar{M}^{(e)} = \begin{bmatrix} 0 & 0 \\ \cdot & \cdot \\ 0 & 0 \\ 1 & 0 \\ 0 & 1 \\ 0 & 0 \\ \cdot & \cdot \\ 0 & 0 \end{bmatrix}_{81 \times 2} \quad m^{th} \text{ row}, n^{th} \text{ row}, \bar{u}^{(e)} = \begin{bmatrix} u_1 \\ u_2 \\ u_3 \\ u_4 \\ \cdot \\ \cdot \\ u_{80} \end{bmatrix}_{81 \times 1}$$

In similar manner Eqs. (31) and (32) are solved using linear elements leading again a 81×81 system respectively.

Consequently, the system of linear algebraic equations illustrated below is obtained.

$$[\bar{K}]_{(243 \times 243)} \bar{U} + [\bar{N}]_{(243 \times 243)} \frac{\partial \bar{U}}{\partial t}_{(243 \times 1)} = [\bar{F}]_{(243 \times 1)}. \tag{51}$$

Here, \bar{U} is given by $\begin{bmatrix} \bar{u} \\ \bar{v} \\ \bar{b} \end{bmatrix}$, system matrices are shown as \bar{K} and \bar{N} and the characteristic vector \bar{F} .

Utilizing the MATLAB program, the Crank-Nicolson method is employed to solve the system.

Table

For the purpose of resolving the proposed problem (51), these physiological variables are employed.

Findings and Discussion

Calcium, buffer and IP₃ fluctuation is depicted in Fig. 1. Calcium fluctuation relative to space is seen in Fig. 1A. The calcium concentration is first high near the source and then starts to decline as one moves along the spatial dimension until it achieves its equilibrium concentration. The maximum calcium content is approximately 0.8 μM. Graph shows non-linear behavior of the calcium concentration pattern between $x = 0$ to 10 μm. This may be due to major imbalances among biophysical processes like diffusion, buffering, efflux and influxes which is clear from the major difference in calcium concentration at $x = 0$ and $x = 10 \mu m$. Calcium variation over time is shown in Fig. 1B. The graph shows that the calcium concentration initially rises abruptly up to around 80 ms, then rises steadily and smoothly until it reaches steady state at approximately 80 ms. The spatial variation of IP₃ concentration is depicted in Fig. 1C. It has been noted that the graph initially behaves nonlinearly before eventually changing to linear behavior. As one moves through space away from the source, the concentration of IP₃ decreases until it reaches $\approx 0.16 \mu M$. Close to the source, the concentration of IP₃ is high. The IP₃ concentrations can reach a maximum value of $\approx 3 \mu M$. The fluctuation of IP₃ concerning time is shown in Fig. 1D. According to the graph, the initial IP₃ concentration increases swiftly for the first 100 ms or so before rising steadily and gradually until it reaches steady state at around 100 ms. Figure 1E displays the variation in free buffer concentration over space. Because too much calcium is toxic for cells, calcium-bound buffer is formed when free buffer and free calcium bond together. Since calcium concentrations are higher close to the source, more buffer is required to lower calcium concentrations there. The free buffer value is therefore lowest close to the source. Buffer diffuses to the calcium source, whereas calcium diffuses to the other end of the cell. Therefore, it is seen that the buffering process is dominated by the source influx of free calcium close to the source, whereas the buffering process is dominated by the calcium signals at the opposite end of the boundary. The fluctuation in free buffer concentration over time is depicted in Fig. 1F. Free buffer concentration first rises steadily and gradually for 500 ms before reaching steady state.

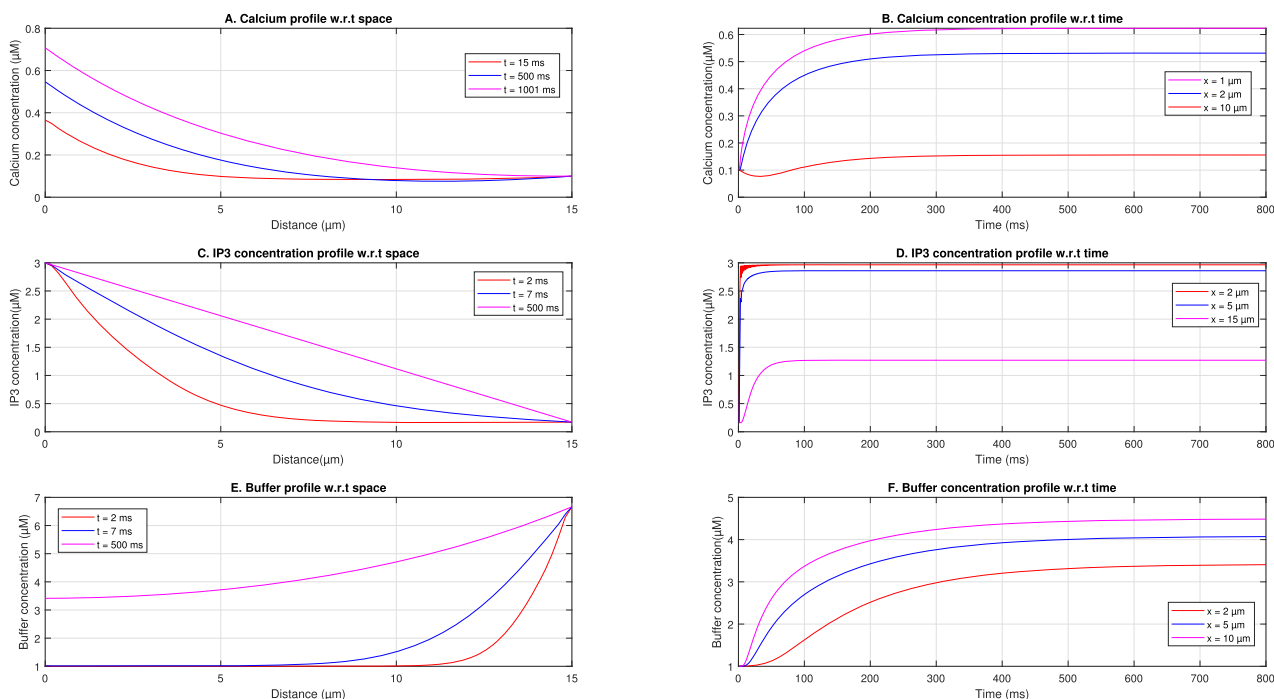


Fig. 1 Ca^{2+} , IP_3 and buffer concentration dynamics along space and time

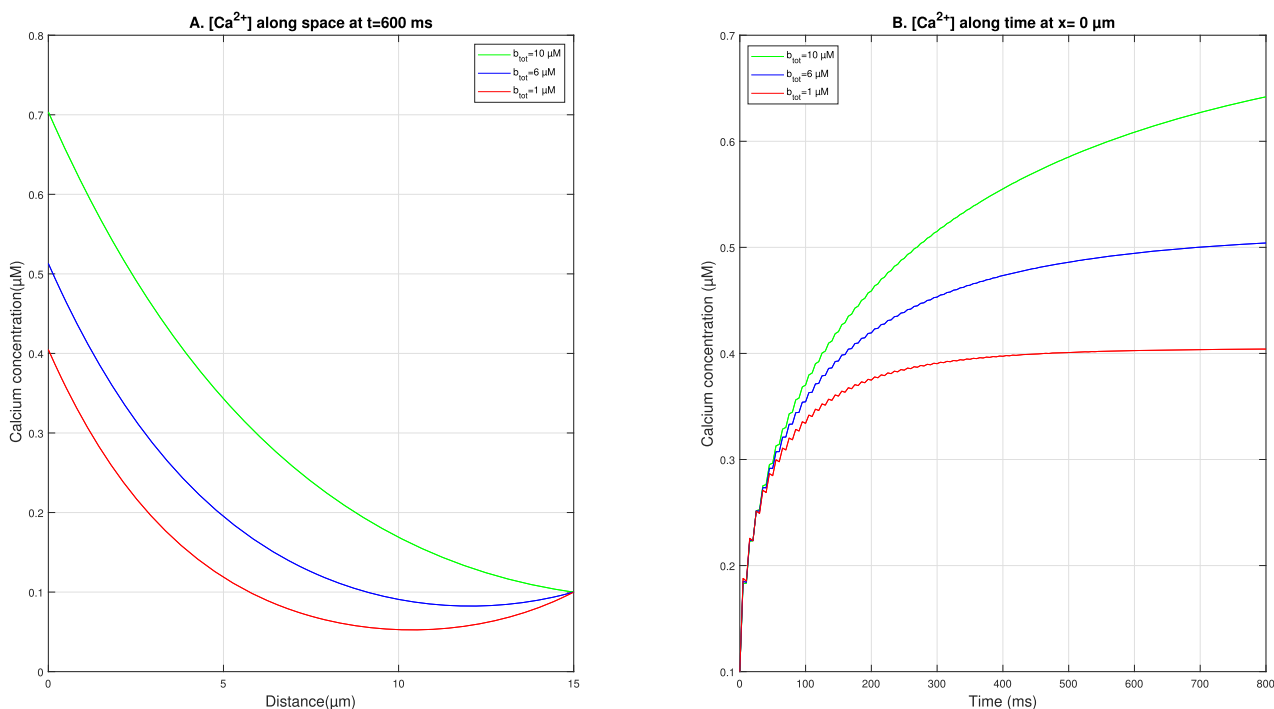


Fig. 2 Ca^{2+} concentration dynamics along space and time for various values of total buffer concentration

Figure 2 shows $[Ca^{2+}]$ variations for different b_{tot} values along space and time. Figure 2A depicts a map of the variation in $[Ca^{2+}]$ with regard to space. As the levels of total buffer concentration rise, a drop in calcium concentration is observed. Calcium concentration falls as a

result of an increase in the amount of calcium-bound buffer caused by an increase in buffer's overall value. $[Ca^{2+}]$ is highest close to the source, and it reaches equilibrium as one moves away from it. The fluctuation in $[Ca^{2+}]$ with respect to time is depicted in Fig. 2B. The concentration of calcium

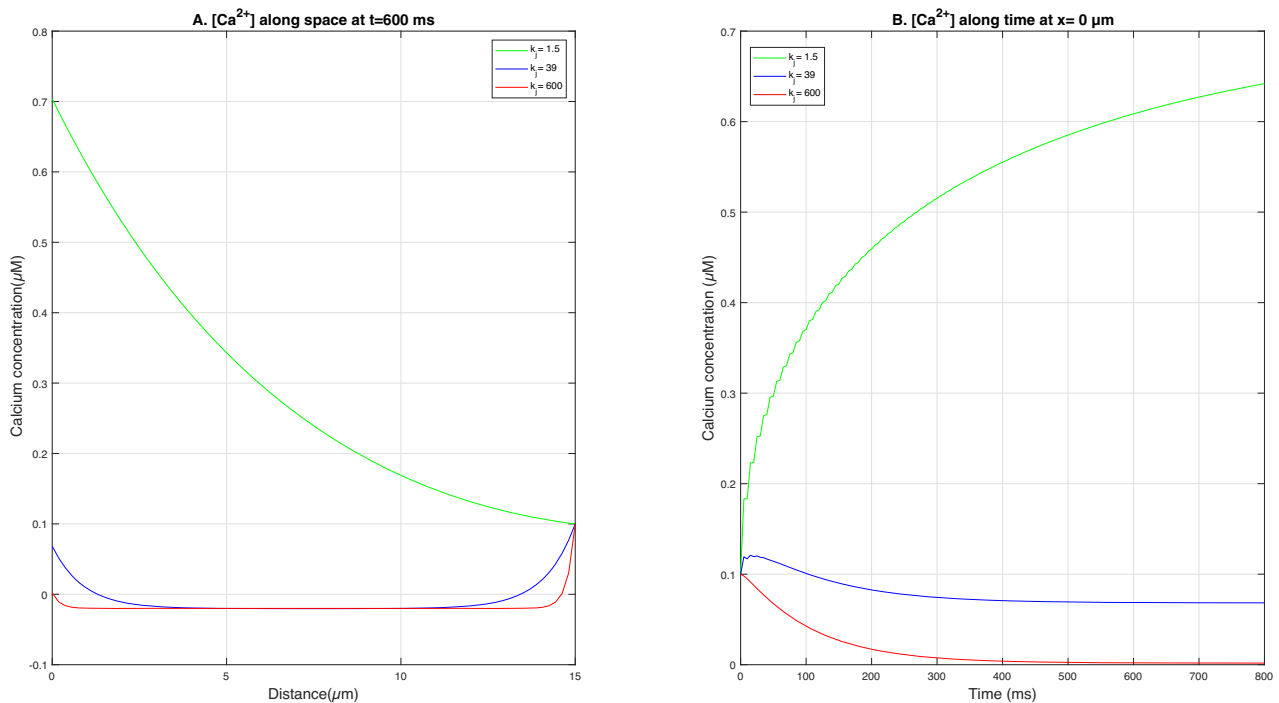


Fig. 3 Ca^{2+} concentration dynamics along space and time for various buffer association rates

first rises quickly until 350 ms, at which point it stabilizes. The fluctuation in calcium concentration exhibits the same behavior as that depicted in Fig. 1.

Figure 3 illustrates $[Ca^{2+}]$ variation over time and space for various association rates of buffers which are BAPTA, EGTA and Triponin C. Figure 3A shows $[Ca^{2+}]$ variation over space. It is demonstrated by comparing the $[Ca^{2+}]$ at the source that it is maximum in the presence of EGTA buffer. Presence of BAPTA buffer changes the behavior of $[Ca^{2+}]$ dynamics and Triponin C reduced $[Ca^{2+}]$ by 90% as association rate for BAPTA and Triponin C are very high. Fig. 3B illustrates the variation in calcium content over time. The results show that the addition of EGTA causes the calcium concentration to rise sharply and gradually up to 350 ms before stabilizing. Triponin C and BAPTA buffers allow to achieve a steady state in 30 ms. The presence of BAPTA and triponin C buffers causes oscillations.

Figure 4 illustrates $[Ca^{2+}]$ variation over space and time for different buffers's diffusion coefficient (D_b). Figure 4A illustrates how the $[Ca^{2+}]$ varies along space. It has been demonstrated that with increase in D_b values, $[Ca^{2+}]$ decreases, leading to an increase in the generation of calcium-bound buffers. Calcium has its maximum concentration near the source and approaches equilibrium farther away. The calcium concentration fluctuation with time is shown in Fig. 4B. Prior to reaching a steady state at 1800 ms, the concentration of calcium first increases swiftly. The small oscillation in the curves are due to formation of Ca^{2+}

bound buffer's binding time and diffusion of free buffer and Ca^{2+} towards each other.

Figure 5 illustrates variation in ATP degradation rates across space and time. Figure 5A demonstrates that the ATP degradation rate is highest at the source and diminishes progressively with distance as. This spatial trend in ATP degradation mirrors the non-linear pattern due to major imbalances among biophysical processes like diffusion, buffering, efflux and influxes as observed in Fig. 1A. Figure 5B details the temporal dynamics of ATP degradation, showing a sharp initial increase up to 200 ms, followed by a more gradual increase to reach steady state after 200 ms. This temporal pattern of ATP degradation shares similarities with the temporal fluctuations of calcium observed in Fig. 1B.

Figure 6 depicts production rate of NADH along space and time. Figure 6A, the spatial distribution of NADH production rate shows a trend where higher calcium concentrations correspond to elevated NADH production rates, gradually stabilizing to around $0.38 \mu M/sec$ as distance from the source increases. This non-linear relationship due to major imbalances among biophysical processes like diffusion, buffering, efflux and influxes mirrors the behavior of Ca^{2+} variation as depicted in Fig. 1A. In Fig. 6B, the temporal dynamics of production rate of NADH reveal an initial sharp increase up to 200 ms, followed by a more gradual and smooth rise, eventually reaching a steady state by 200 ms. This temporal pattern of NADH production rate

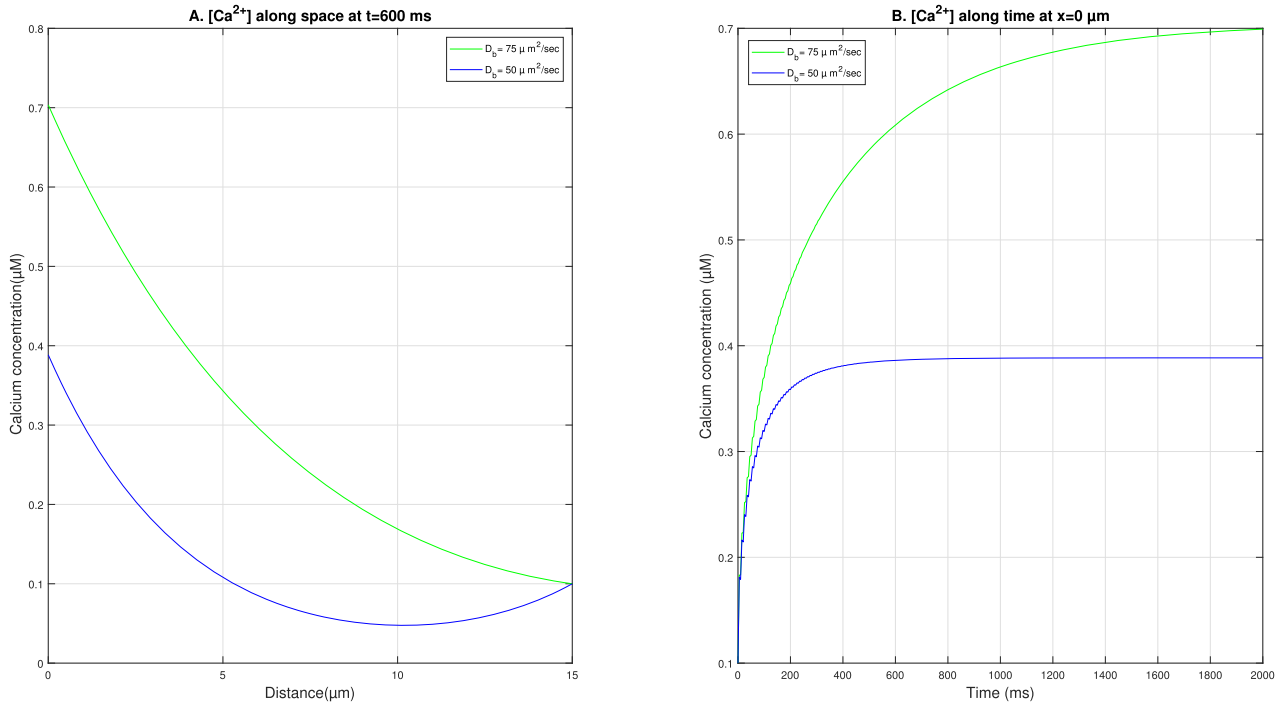


Fig. 4 Ca²⁺ concentration dynamics along space and time for various values of diffusion coefficient of buffer

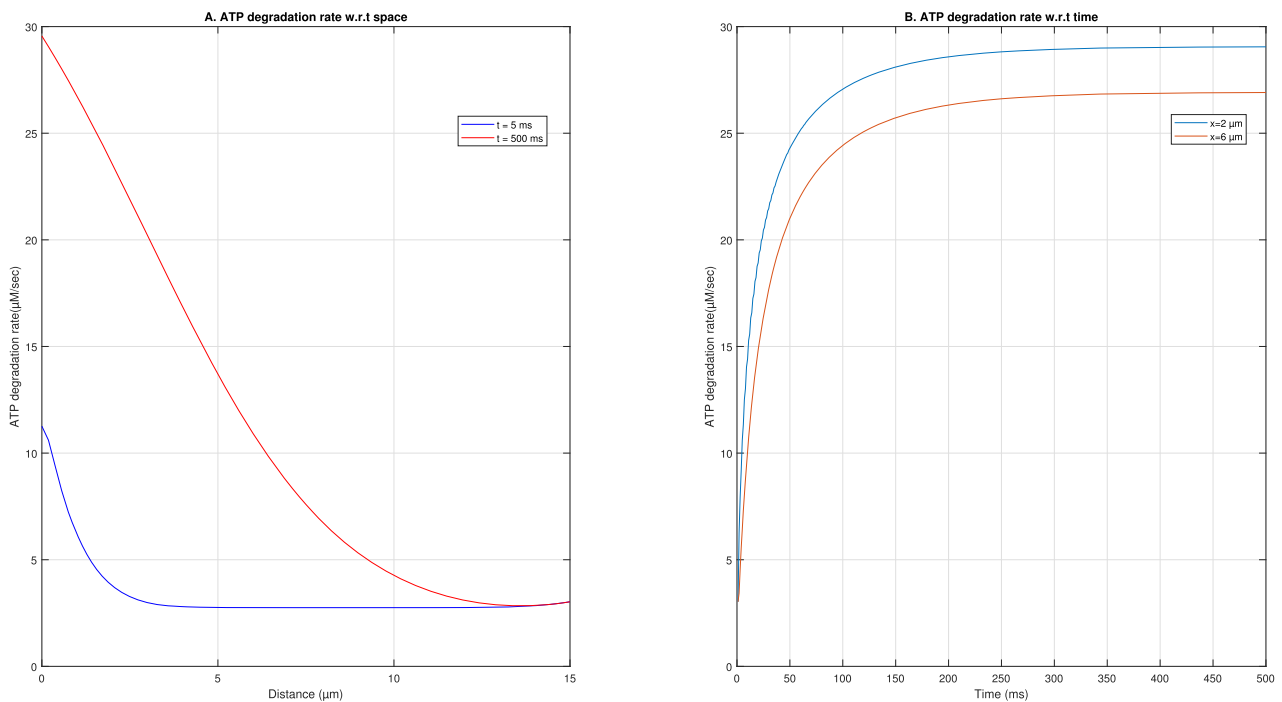


Fig. 5 ATP degradation dynamics along space and time

closely resembles the temporal behavior of Ca²⁺ variation illustrated in Fig. 1B.

Figure 7 displays spatial and temporal Ca²⁺-dependent ATP production rate. Figure 7A shows variation in calcium-dependent production rate of ATP along space. Near source

Ca²⁺-dependent production rate of ATP is high and decreases upto 0.18 μM/sec moving away from the source. Maximum calcium-dependent ATP production rate is ≈ 0.7 μM/sec. The non-linear behavior due to major imbalances among biophysical processes like diffusion, buffering,

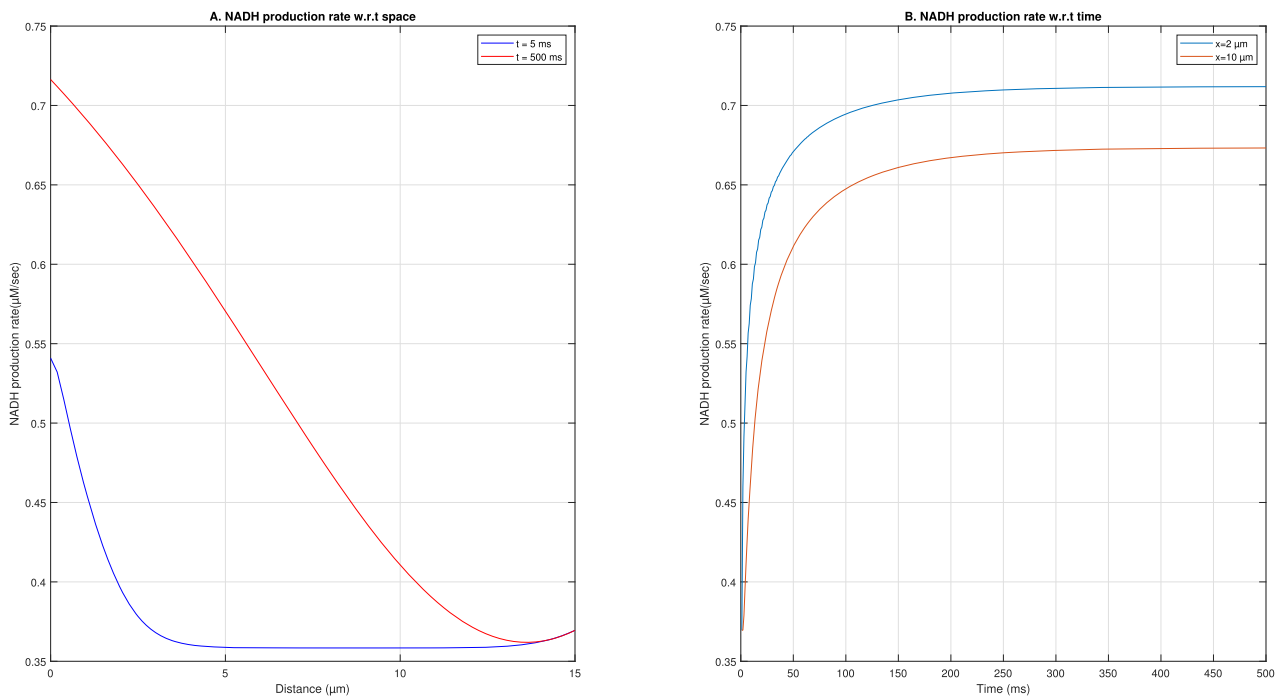


Fig. 6 NADH production dynamics along space and time

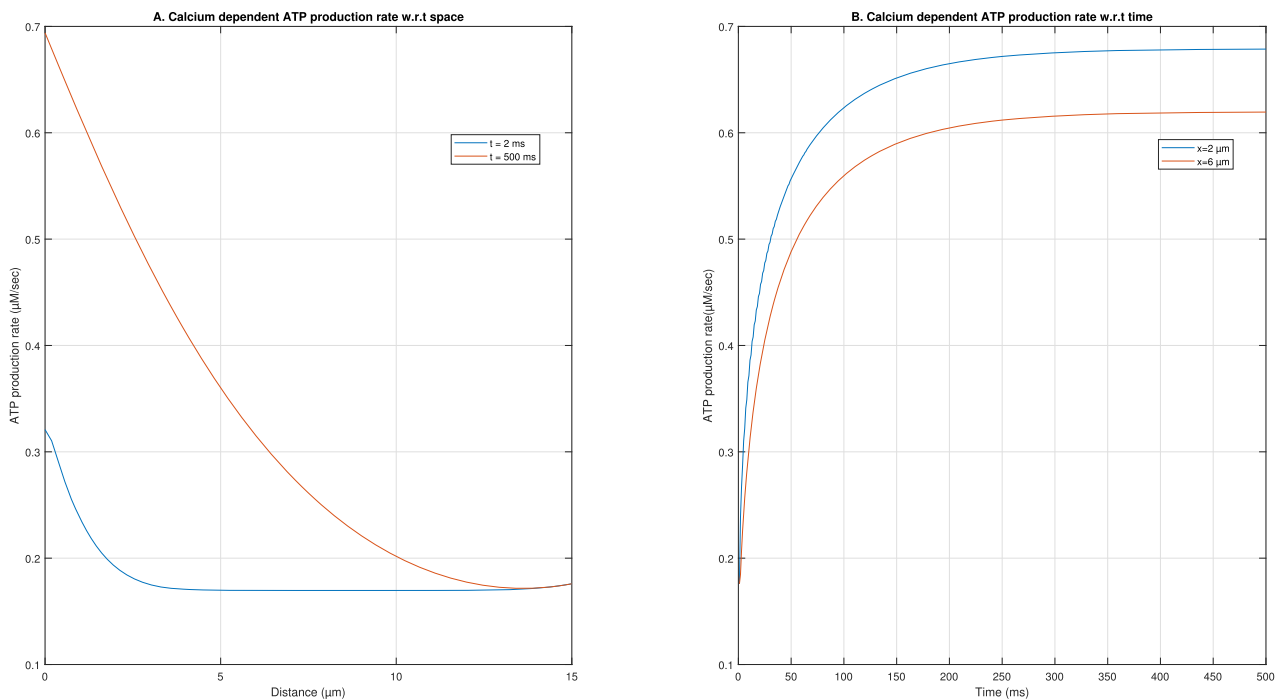


Fig. 7 Ca²⁺ dependent ATP production dynamics along space and time

efflux and influxes mirrors the behavior of Ca²⁺ variation as depicted in Fig. 1A. Figure 7B shows the rate of Ca²⁺-dependent ATP synthesis over time. The graph shows that, at first, the Ca²⁺-dependent ATP production rate increases quickly up to ≈ 200 ms, after which it grows steadily and

smoothly to reach steady state at almost 200 ms. The calcium variation’s nonlinear behavior in Fig. 1 and the ATP generation rate in Fig. 7 exhibit synergistic effects.

Figure 8 shows spatial and temporal IP₃-dependent ATP production rate. Figure 8A shows variation in IP₃-

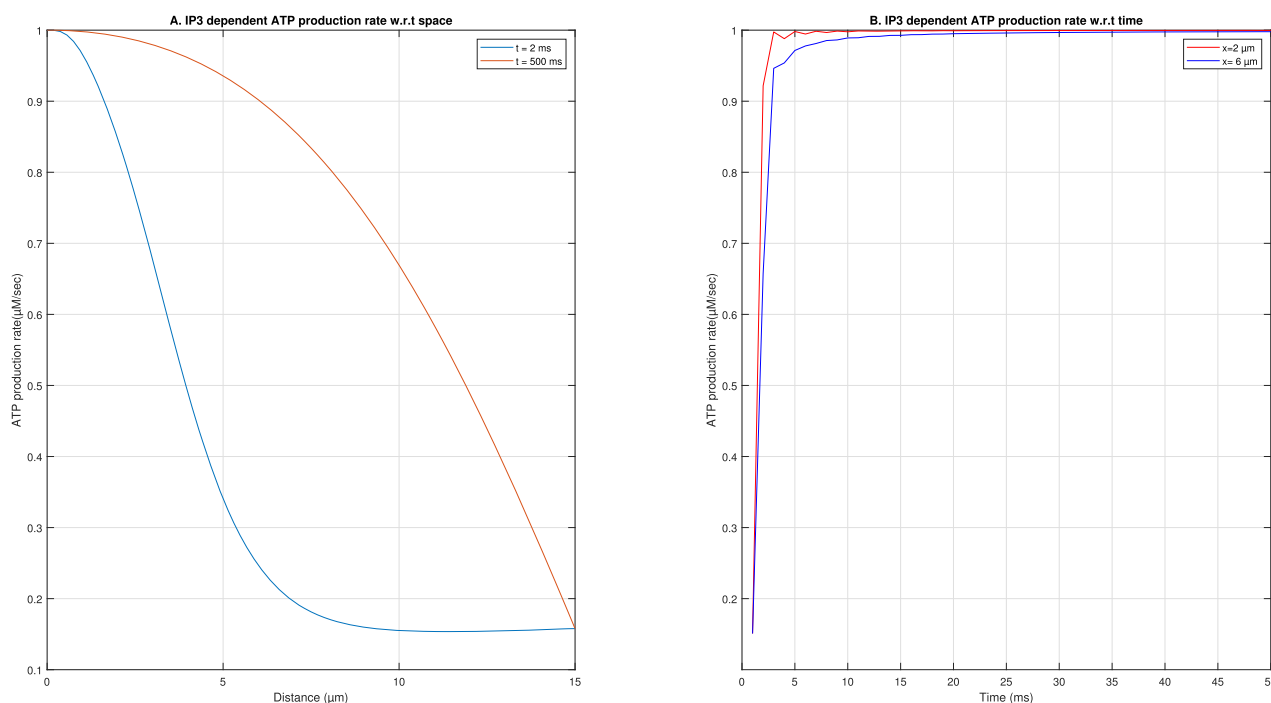


Fig. 8 IP₃ dependent ATP production dynamics along space and time

dependent production rate of ATP along space. Near the source IP₃-dependent ATP production rate is high and decreases upto 0.18 $\mu\text{M}/\text{sec}$ moving away from the source. Maximum IP₃-dependent ATP production rate is $\approx 1 \mu\text{M}/\text{sec}$. The non-linear behavior is similar to Fig. 1A initially as time increases such as 500 ms behavior of the curves changes and becomes concave. This change in behavior of the curves is due to role of increase in calcium concentration on IP₃ and ATP production. Initially when calcium concentration is low, the IP₃ concentration is also lower and ATP production rate is also lower and with the passage of time, calcium concentration increases and its effect is visible on IP₃ profiles in Fig. 1C and on ATP production in Fig. 8A. Also after sometime such as 500 ms, the calcium concentration becomes high enough to play significant role which is visible by change in behavior of curves in Figs. 1A and 8A. Figure 8B represents IP₃-dependent production rate of ATP with respect to time. The graph demonstrates how the initial IP₃-dependent ATP production rate grows abruptly up to ≈ 20 ms, then rises gradually and smoothly until it takes ≈ 20 ms to reach steady state.

The variations in calcium concentration for both normal and obese hepatocyte cells across time and space are shown in Fig. 9. The fluctuations in $[\text{Ca}^{2+}]$ with respect to space is shown in Fig. 9A. It has been noted that increased ER leakage causes an increase in calcium concentration in obese hepatocyte cells. $[\text{Ca}^{2+}]$ is highest close to the source and decreases to the background level (0.1 μM) as one moves away. Moreover, the temporal fluctuation in calcium

concentration for normal and obese hepatocyte cells is shown in Fig. 9B. The fluctuations in the calcium concentration exhibit behavior that is in line with the observations shown in Fig. 1A and B. A notable variation in the calcium content is seen from the curves in Fig. 9 for the two distinct scenarios.

The change in the rate of ATP breakdown for normal and obese hepatocyte cells over time and space is shown in Fig. 10. The spatial variation in ATP degradation rate for normal and obese hepatocyte cells is shown in Fig. 10A. It is demonstrated from the figure that how the rate of ATP breakdown increases in tandem with the amounts of calcium in the obese hepatocyte cell as the ER becomes leaky. The rate of ATP degradation peaks at the source and falls away from it to a constant value of 4 $\mu\text{M}/\text{sec}$. The variation in the rate of ATP breakdown for both normal and obese hepatocyte cells over time is shown in Fig. 10B. Figure 10 illustrates a large variation in the rate of ATP breakdown for two distinct scenarios. The ATP degradation rate variation behaves similarly to Fig. 9.

The variation in the rate of NADH synthesis in a obese and normal hepatocyte cell over time and space is depicted in Fig. 11. The spatial variation in the rate of NADH synthesis for normal and obese hepatocyte cells is shown in Fig. 11A. The figure shows that as compared to a normal hepatocyte cell, the rate of NADH synthesis rises in the obese state as the ER becomes leaky. The decrease in the rate of NADH generation for both normal and obese hepatocyte cells over time is shown in Fig. 11B. Two different scenarios with different rates of NADH generation are depicted in Fig. 11. According to Fig. 9, the NADH production rate fluctuation acts similarly.

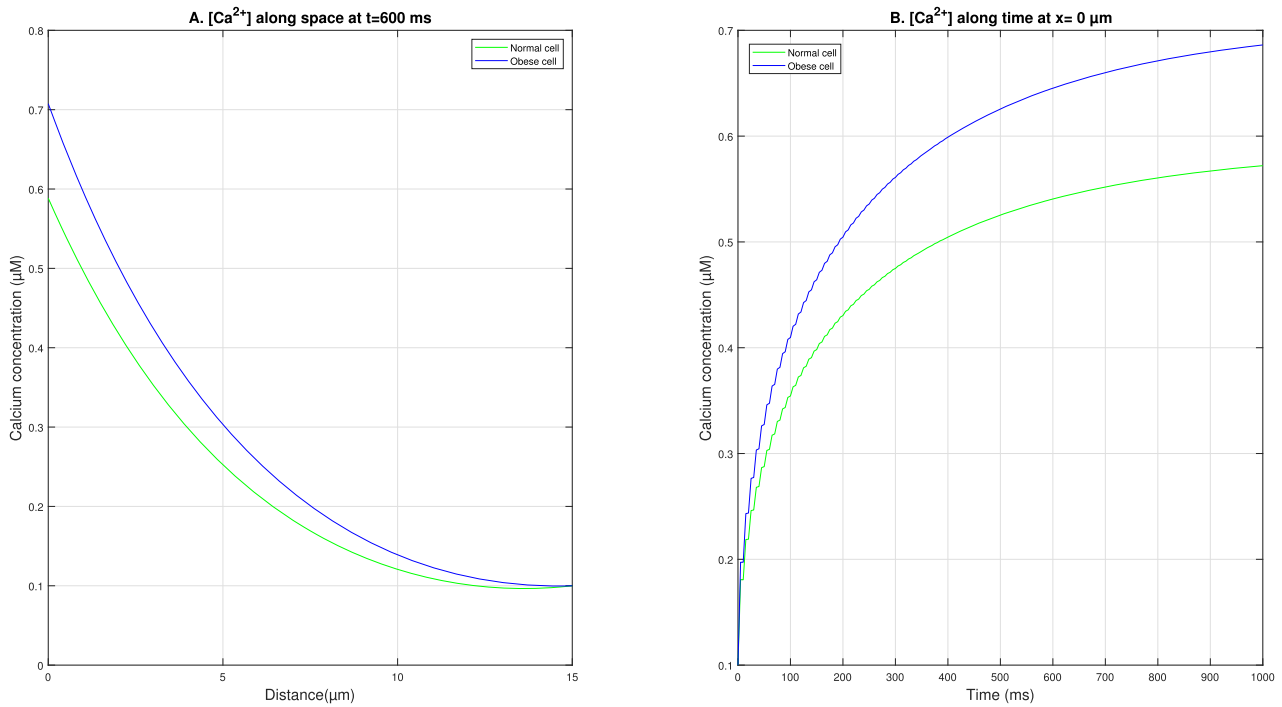


Fig. 9 Ca²⁺ dynamics for normal and obese cell along space and time

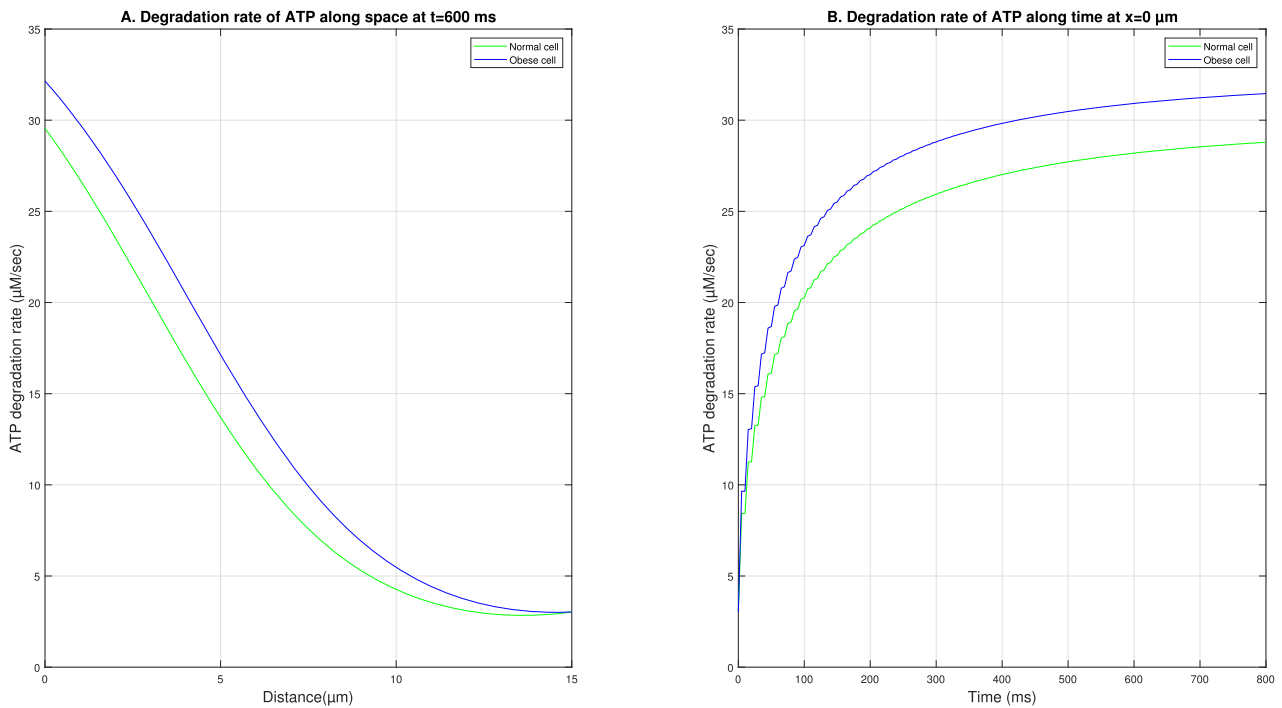


Fig. 10 ATP degradation rate dynamics for normal and obese cell with respect to space and time

The calcium-dependent ATP generation rate variation for normal and obese hepatocyte cells over time and space is shown in Fig. 12. Figure 12A illustrates the variation in the rate of Ca²⁺-dependent ATP synthesis in relation to

space in a obese and normal hepatocyte cells. Figure shows how the rate of calcium-dependent ATP production increases in an obese hepatocyte cell in tandem with an increase in calcium concentration when the ER

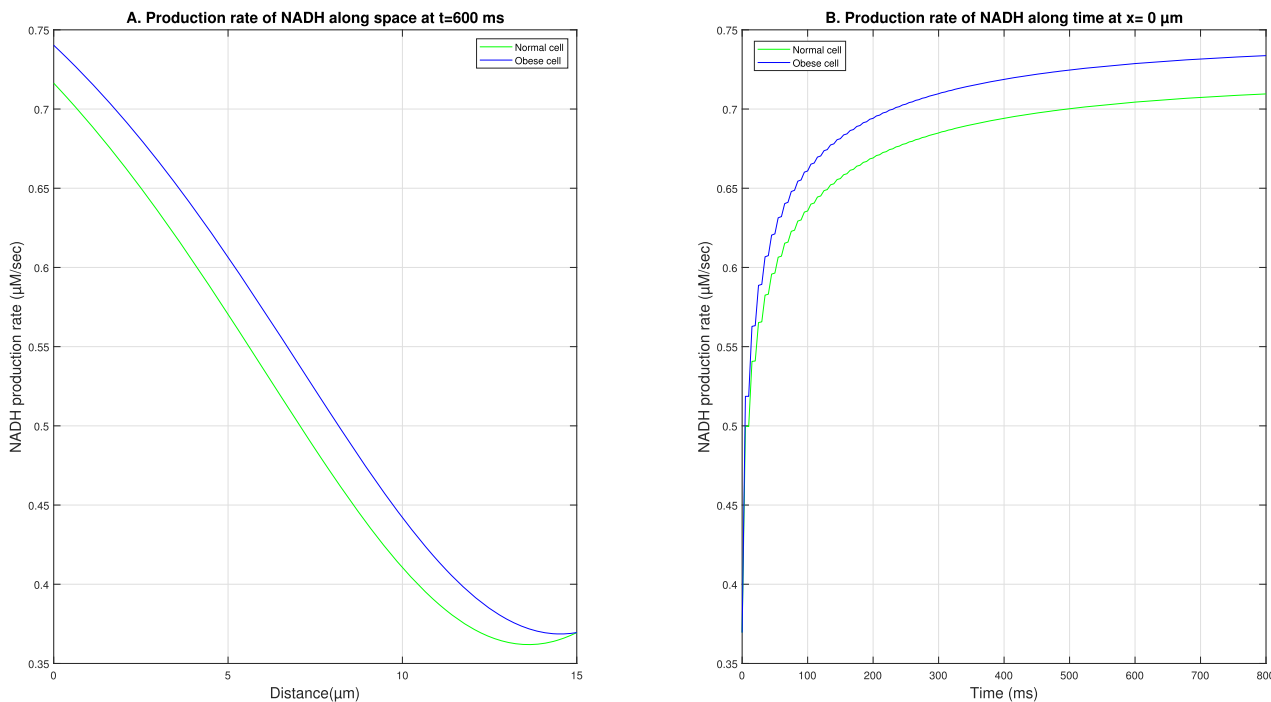


Fig. 11 Production rate of NADH dynamics for normal and obese cell along space and time

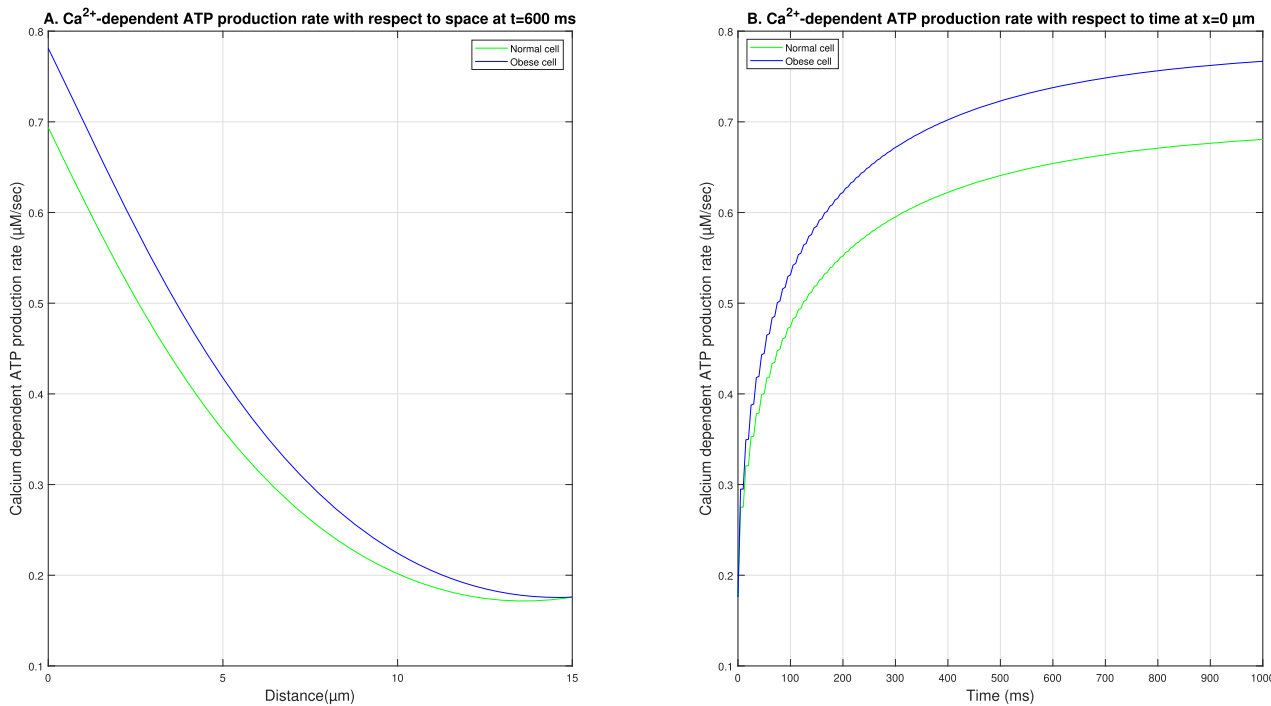


Fig. 12 Ca²⁺- dependent production rate of ATP dynamics for obese and normal cell over space and time

becomes leaky. The rate at which calcium-dependent ATP is produced reaches its maximum near the source and falls away from it to a stable value of 0.2 µM/sec. The calcium-dependent ATP generation rate changes with

time for both normal and obese hepatocyte cells are shown in Fig. 12B. The ATP generation rates for two distinct circumstances are displayed in Fig. 12, each of which exhibits a notable variance. The behavior of the

Table 1 Ca²⁺, IP₃ and buffer variation parameters [32, 57]

Symbol	Parameter	Value
D_{Ca}	Diffusion coefficient of calcium	16 $\mu m^2/sec$
D_b	Buffer's diffusion coefficient	75 $\mu m^2/sec$
D_I	IP ₃ 's diffusion coefficient	283 $\mu m^2/sec$
C_∞	Calcium concentration at equilibrium	0.1 μM
V_c	Volume ratio of the cytosol to the overall volume of the cell	0.83
K_{IP3R}	Activating IP ₃ binding site's dissociation constant	0.3 μM
CT	Total calcium concentration	2 μM
V_e	The ER's volume in relation to the overall cell volume	0.17
K_{SERCA}	Half maximal rate of SERCA	0.1 μM
k_j^+	Buffer(EGTA) association rate	1.5 $(\mu M/s)^{-1}$
k_j^-	Buffer(EGTA) dissociation rate	0.3 sec^{-1}
b_{tot}	Total buffer concentration	10 μM
V_{IP3R}	Flux rate of IP ₃ receptor	1.5 sec^{-1}
V_{Leak}	Flux rate of ER leakage	0.01 sec^{-1}
V_{SERCA}	Flux rate of SERCA pump	0.65 sec^{-1}
K_{Act}	Ca ²⁺ activation binding site dissociation constant	0.8 μM
K_{Inh}	Dissociation constant of Ca ²⁺ inhibiting binding site	1.9 μM
V_{Prod}	Maximum production rate of IP ₃	0.075 $\mu M/sec$
K_{Prod}	Ca ²⁺ activation Michaelis constant	0.4 μM
λ	Scaling factor for the production rate in IP ₃	30
V_1	Maximum rate constant at low Ca ²⁺ (3-kinase)	0.001 $\mu M/sec$
V_2	Maximum rate constant (at high Ca ²⁺ (3-kinase))	0.005 $\mu M/sec$
V_3	Highest rate constant (phosphatase)	0.02 $\mu M/sec$
V_{AGC}	NADH production rate constant	25 $\mu M/sec$
K_{AGC}	Ca ²⁺ 's dissociation constant from AGC	0.14 μM
c_m	Mitochondrial calcium concentration	1.3 μM
F_0	Constant (ATP feedback)	0.5
G_0	Constant (ATP feedback)	0.5
$[Ca^{2+}]_{max}$	Constant (ATP feedback)	1.5 mM
V_{max}	Constant (ATP feedback)	1.5 mM
V_M	Mitochondrial membrane potential	160mV
p_4	Voltage dependence coefficient of AGC activity	0.01 m V ⁻¹
q_2	Value for activation the Krebs cycle by Ca ²⁺	0.1 μM

Ca²⁺-dependent ATP production rate fluctuation is similar to that of Ca²⁺, as seen in Fig. 9.

Error Analysis

For time =0.1, 0.2, 0.3, 0.4, and $t = 0.5$ sec at $x=0$, error analysis is carried out Tables 1 and 2. According to Tables 3, 4 and 5, the greatest percentage error between nodes 80 and 90 for calcium, IP₃ and buffer dynamics is 0.048172601%, 0.22712485% and 0.001948211%, respectively. The accuracy of the finite element approach with 80 linear elements is found to be 99.95% for the calcium profile, 99.77% for the IP₃ profile and 99.99% for buffer profile in this problem.

Table 2 Comparative study [70]

Symbol	Normal cell	Obese cell
K_{IP3R}	0.3 sec^{-1}	0.35 sec^{-1}

Table 3 Calcium profile error analysis with 80 & 90 elements

Time	Elements = 80	Elements = 90	Relative % error
0.1 sec	0.37017202	0.369890149	0.048172601
0.2 sec	0.458896003	0.458672369	0.038219612
0.3 sec	0.515066144	0.514913538	0.026080804
0.4 sec	0.555023353	0.554925782	0.01667521
0.5 sec	0.58512786	0.58506805	0.010221765

Table 4 IP₃ profile error analysis with 80 & 90 elements

Time	Elements = 80	Elements = 90	Relative % error
0.1 sec	2.959012353	2.965745843	0.22712485
0.2 sec	2.964470144	2.969782735	0.179197046
0.3 sec	2.96544568	2.970238503	0.161664945
0.4 sec	2.96514116	2.969716402	0.154325821
0.5 sec	2.964664378	2.96912403	0.150426894

Table 5 Buffer concentration profile's error analysis with 80 & 90 elements

Time	Elements = 80	Elements = 90	Relative % error
0.1 sec	1.021262566	1.02126464	0.000126852
0.2 sec	1.071696957	1.071725058	0.001718173
0.3 sec	1.211217292	1.211257353	0.002449443
0.4 sec	1.413639489	1.413677127	0.002301281
0.5 sec	1.635500543	1.635532407	0.001948211

Stability Analysis

The finite element approach has a spectral radius of 0.9994 which is below one, indicating that it is stable.

Validation

The results are similar with earlier study by Wagner and Pawar et al. [45, 48] at time $t = 50$ sec, as shown in Tables 6 and 7. The concentration profiles of $[Ca^{2+}]$ and IP₃ that were obtained for the parameter at $x = 0, 3, 6, 9, 12$ and 15 μm are compared to these results.

Table 6 $[Ca^{2+}]$ profiles compared with Wagner and Pawar et al. [45, 48]

Distance	$[Ca^{2+}]$ (Wagner et al.)	$[Ca^{2+}]$ (Pawar et al.)	$[Ca^{2+}]$ (Current work)
$x=0 \mu m$	1.332308069	1.34981836731882	1.336291832
$x=3 \mu m$	1.194347794	1.19298936853484	1.190632459
$x=6 \mu m$	1.022311435	1.01607655910625	1.015763902
$x=9 \mu m$	0.809486385	0.795809556080343	0.804011992
$x=12 \mu m$	0.529051723	0.503248604412665	0.526519714
$x=15 \mu m$	0.1	0.1	0.1

Table 7 IP_3 concentration profiles compared with Wagner and Pawar et al. [45, 48]

Distance	IP_3 (Wagner et al.)	IP_3 (Pawar et al.)	IP_3 (Current work)
$x=0 \mu m$	0.5	0.5000	0.5
$x=3 \mu m$	0.436618677	0.431787350767981	0.438932358
$x=6 \mu m$	0.36738949	0.363691496147387	0.372099536
$x=9 \mu m$	0.299355639	0.295702458806600	0.306262011
$x=12 \mu m$	0.232442228	0.227809393499215	0.241362587
$x=15 \mu m$	0.16	0.16	0.16

Conclusion

A mathematical model of cross talking dynamics of calcium, buffers and IP_3 is proposed and successfully implemented to study impacts of spatio temporal variations in one of them on the other two signaling molecules. The outcomes of the simulations lead to the following fundamental conclusions:

- (i) $[Ca^{2+}]$ increases with increase in source influx and consequently IP_3 increases.
- (ii) Calcium concentration decreases with increasing buffer value and consequently IP_3 decreases.
- (iii) Calcium has the maximum concentration near the source and approaches equilibrium when one travels farther away from it in space. For IP_3 , comparable outcomes are attained.
- (iv) According to temporal study, the calcium concentration initially rises abruptly for about 450 ms before rising gradually and smoothly until it reaches a steady state. Similar results are obtained for IP_3 .

The above basic conclusions are the same as obtained by earlier researchers [9, 45] which indicate that the proposed model is effective in prediction of experimental results.

The following novel findings are reached by analyzing numerical results:

- (i) The free buffer concentration falls till $x=10 \mu m$ as a result of strong buffering activity which lowers the free $[Ca^{2+}]$ at those places ($x=0$ to $10 \mu m$) and thus the spatial regions with high calcium concentrations also have low free buffer concentrations.
- (ii) The concentration of free buffer rises slowly in the spatial places ($x=1$ to $10 \mu m$) where the concentration of calcium rises the fastest because the majority of free buffer binds to free calcium. The calcium concentration rises slowly in the same way that it does wherever the buffer concentration is rising quickly.
- (iii) Depending on where each of the calcium, IP_3 and buffers dominates at different times, it leads to the variations in concentration levels of the other two signaling molecules. Thus these three signaling systems work in a synergistic manner to balance each others fluctuations to achieve the homeostasis.
- (iv) The dynamic relationship between the fluctuations of free buffer and free calcium is determined by the rate of a modest increase in buffer activity.
- (v) Source, buffer, SERCA pump and other parameters that affect calcium profiles are synergistically conveyed to IP_3 , ATP degradation, ATP synthesis and NADH production rate. Therefore, changes in these parameters can result in considerable variations in the rates of ATP generation, ATP degradation and NADH production which can result in a variety of liver illnesses like obesity, diabetes etc.
- (vi) The significant discrepancy in calcium concentration, ATP production, degradation and NADH production rate in a obese and normal hepatocyte cell has provided us with new insight into the severity of the disorder in the form of obesity, among other things.
- (vii) As ER calcium content drops by 50% in case of obesity, ER calcium release rises by 50%. According to Arruda et al. [69], mitochondria receive 80% of the inflow from the ER. This led to the prediction that a hepatocyte cell's cytoplasmic calcium concentration would only rise by 10%, as seen in Fig. 9.

The finite element method (FEM) showcases remarkable versatility, yet grapples with mesh dependency, complexity in 3D scenarios, and challenges in handling discontinuities. Meanwhile, the Crank-Nicolson method, lauded for its stability, contends with constraints in stability, computational overhead, and accuracy, particularly in nonlinear domains. Both methods demand finesse in implementation, with FEM demanding meticulous meshing and Crank-Nicolson necessitating careful consideration of system dynamics. Despite these limitations, their combined prowess remains a cornerstone in numerical simulations, driving innovation across diverse fields of science and

engineering. Consequently, the proposed model demonstrates a commendable ability to accurately estimate calcium concentration levels in both normal and obese cellular conditions. Additionally, the model demonstrates the ability to forecast the impacts of diverse variable alterations on calcium, buffer and IP₃ concentrations, alongside NADH generation, ATP biosynthesis and ATP degradation rate within hepatocyte cells, across both normal and obese states. This predictive capability enhances our understanding of the intricate cellular dynamics and provides valuable insights into the physiological implications of these changes in calcium and energy-related processes.

Data Availability

No datasets were generated or analysed during the current study.

Author Contributions We both the authors equally contributed in this paper in terms of formulation of problem, solution, data correction/literature review and interpretation of the results. The MATLAB program is developed by author (1).

Competing interests The authors declare no competing interests.

References

- Barritt, G. J., Chen, J., & Rychkov, G. Y. (2008). Ca²⁺-permeable channels in the hepatocyte plasma membrane and their roles in hepatocyte physiology. *Biochimica et Biophysica Acta*, 1783, 651–672.
- Pierobon, N., Renard-Rooney, D. C., Gaspers, L. D., & Thomas, A. P. (2006). Ryanodine receptors in liver. *Journal of Biological Chemistry*, 281, 34086–34095.
- Hirata, K., Pusch, T., O'Neill, A. F., Dranoff, J. A., & Nathanson, M. H. (2002). The type II inositol 1, 4, 5-trisphosphate receptor can trigger Ca²⁺ waves in rat hepatocytes. *Gastroenterology*, 122, 1088–1100.
- Jha, A., & Adlakha, N. (2014). Finite element model to study the effect of exogenous buffer on calcium dynamics in dendritic spines. *The International Journal of Modeling, Simulation, and Scientific Computing*, 5, 1350027.
- Jha, A., Adlakha, N., & Jha, B. K. (2016). Finite element model to study effect of Na⁺-Ca²⁺ exchangers and source geometry on calcium dynamics in a neuron cell. *Journal of Mechanics in Medicine and Biology*, 16, 1650018.
- Jagtap, Y., & Adlakha, N. (2019). Numerical study of one-dimensional buffered advection-diffusion of calcium and IP₃ in a hepatocyte cell. *Network Modeling Analysis in Health Informatics and Bioinformatics*, 8, 25.
- Kotwani, M., & Adlakha, N. (2017). Modeling of endoplasmic reticulum and plasma membrane Ca²⁺ uptake and release fluxes with excess buffer approximation (EBA) in fibroblast cell. *International Journal of Computational Materials Science*, 6, 1750004.
- Naik, P. A., & Pardasani, K. R. (2015). One dimensional finite element model to study calcium distribution in oocytes in presence of VGCC, RyR and buffers. *Journal of Medical Imaging and Health Informatics*, 5, 471–476.
- Panday, S., & Pardasani, K. R. (2013). Finite element model to study effect of advection diffusion and Na⁺/Ca²⁺ exchanger on Ca²⁺ distribution in oocytes. *Journal of Medical Imaging and Health Informatics*, 3, 374–379.
- Pathak, K. B., & Adlakha, N. (2015). Finite element model to study calcium signalling in cardiac myocytes involving pump, leak and excess buffer. *Journal of Medical Imaging and Health Informatics*, 5, 683–688.
- Tewari, S. G., & Pardasani, K. R. (2012). Modeling effect of sodium pump on calcium oscillations in neuron cells. *Journal of Multiscale Modelling*, 4, 1250010.
- Kotwani, M., Adlakha, N., & Mehta, M. N. (2012). Numerical model to study calcium diffusion in fibroblasts cell for one dimensional unsteady state case. *Applied Mathematical Sciences*, 6, 5063–5072.
- Kotwani, M., Adlakha, N., & Mehta, M. N. (2014). Finite element model to study the effect of buffers, source amplitude and source geometry on spatio-temporal calcium distribution in fibroblast cell. *Journal of Medical Imaging and Health Informatics*, 4, 840–847.
- Bhardwaj, H., & Adlakha, N. (2023). Model to study inter-dependent calcium and IP₃ distribution regulating NFAT production in T lymphocyte. *Journal of Mechanics in Medicine and Biology*, 24, 2350055.
- Bhardwaj, H., & Adlakha, N. (2022). Radial basis function based differential quadrature approach to study reaction diffusion of Ca²⁺ in T Lymphocyte. *International Journal of Computational Methods*. <https://doi.org/10.1142/S0219876222500591>.
- Naik, P. A., & Pardasani, K. R. (2016). Finite element model to study calcium distribution in oocytes involving voltage gated Ca²⁺ channel, ryanodine receptor and buffers. *Alexandria Journal of Medicine*, 52, 43–49.
- Naik, P. A., & Pardasani, K. R. (2019). Three-dimensional finite element model to study effect of RyR calcium channel, ER leak and SERCA pump on calcium distribution in oocyte cell. *International Journal of Computational Methods*, 16, 1850091.
- Naik, P. A. (2020). Modeling the mechanics of calcium regulation in T lymphocyte: a finite element method approach. *International Journal of Biomathematics*, 13, 2050038.
- Kumar, H., Naik, P. A., & Pardasani, K. R. (2018). Finite element model to study calcium distribution in T lymphocyte involving buffers and ryanodine receptors. *Proceedings of the National Academy of Sciences, India Section A: Physical Sciences*, 88, 585–590.
- Naik, P. A., & Pardasani, K. R. (2014). Finite element model to study effect of Na⁺/K⁺ Pump and Na⁺/Ca²⁺ exchanger on calcium distribution in oocytes in presence of buffers. *Asian Journal of Mathematics & Statistics*, 7, 21–28.
- Naik, P. A., & Pardasani, K. R. (2017). Three-dimensional finite element model to study calcium distribution in oocytes. *Network Modeling and Analysis in Health Informatics and Bioinformatics*, 6, 16.
- Naik, P. A., & Pardasani, K. R. (2015). Two dimensional finite element model to study calcium distribution in oocytes. *Journal Multiscale Modelling*, 06, 1756–9737.
- Pathak, K., & Adlakha, N. (2016). Finite element model to study two dimensional unsteady state calcium distribution in cardiac myocytes. *Alexandria Journal of Medicine*, 52, 261–268.
- Jha, B. K., Adlakha, N., & Mehta, M. N. (2014). Two-dimensional finite element model to study calcium distribution in astrocytes in presence of excess buffer. *International Journal of Biomathematics*, 7, 1450031.
- Jha, B. K., Jha, A., & Adlakha, N. (2020). Three-dimensional finite element model to study calcium distribution in astrocytes in presence of VGCC and excess buffer. *Differential Equations and Dynamical Systems*, 28, 603–616.

26. Panday, S., & Pardasani, K. R. (2014). Finite element model to study the mechanics of calcium regulation in oocyte. *Journal of Mechanics in Medicine and Biology*, *14*, 1450022.
27. Jha, A., & Adlakha, N. (2015). Two-dimensional finite element model to study unsteady state Ca^{2+} diffusion in neuron involving ER LEAK and SERCA. *International Journal of Biomathematics*, *8*, 1550002.
28. Manhas, N., & Pardasani, K. R. (2014). Modelling mechanism of calcium oscillations in pancreatic acinar cells. *Journal of Bioenergetics and Biomembranes*, *46*, 403–420.
29. Manhas, N., & Pardasani, K. R. (2014). Mathematical model to study IP_3 dynamics dependent calcium oscillations in pancreatic acinar cells. *Journal of Medical Imaging and Health Informatics*, *4*, 874–880.
30. Tewari, S., & Pardasani, K. R. (2010). Finite element model to study two dimensional unsteady state cytosolic calcium diffusion in presence of excess buffers. *IAENG International Journal of Applied Mathematics*, *40*, 108–112.
31. Jagtap, Y., & Adlakha, N. (2018). Finite volume simulation of two dimensional calcium dynamics in a hepatocyte cell involving buffers and fluxes. *Communications in Mathematical Biology and Neuroscience*, *2018*, 1–16.
32. Jagtap, Y., & Adlakha, N. (2023). Numerical model of hepatic glycogen phosphorylase regulation by nonlinear interdependent dynamics of calcium and IP_3 . *The European Physical Journal - Plus*, *138*, 1–13.
33. Mishra, V., & Adlakha, N. (2023). Numerical simulation of calcium dynamics dependent ATP degradation, IP_3 and NADH production due to obesity in a hepatocyte cell. *Journal of Biological Physics*, *49*, 415–442.
34. Mishra, V., & Adlakha, N. (2023). Spatio temporal interdependent calcium and buffer dynamics regulating DAG in a hepatocyte cell due to obesity. *Journal of Bioenergetics and Biomembranes*, *55*, 249–266.
35. Kothiya, A., & Adlakha, N. (2023). Impact of interdependent Ca^{2+} and IP_3 dynamics on ATP regulation in a fibroblast model. *Cell Biochemistry and Biophysics*, *81*, 795–811.
36. Kothiya, A., & Adlakha, N. (2023). Computational investigations of the Ca^{2+} and TGF- β dynamics in a fibroblast cell. *The European Physical Journal - Plus*, *138*, 1–21.
37. Kothiya, A., Adlakha, N. Mathematical model for system dynamics of Ca^{2+} and dopamine in a fibroblast cell, *Journal of Biological Systems*, 1–28 (2024).
38. Kothiya, A., & Adlakha, N. (2023). Simulation of biochemical dynamics of Ca^{2+} and PLC in fibroblast cell. *Journal of Bioenergetics and Biomembranes*, *55*, 267–287.
39. Vaishali, & Adlakha, N. (2023). Disturbances in system dynamics of Ca^{2+} and IP_3 perturbing insulin secretion in a pancreatic β -cell due to type-2 diabetes. *Journal of Bioenergetics and Biomembranes*, *55*, 151–167.
40. Vaishali, & Adlakha, N. (2024). Model of calcium dynamics regulating IP_3 , ATP and insulin production in a pancreatic β -Cell. *Acta Biotheoretica*, *72*, 2.
41. Hajnoczky, G., & Thomas, A. P. (1997). Minimal requirements for calcium oscillations driven by the IP_3 receptor. *EMBO Journal*, *16*, 3533–3543.
42. Politi, A., Gaspers, L. D., Thomas, A. P., & Hofer, T. (2006). Models of IP_3 and Ca^{2+} oscillations: frequency encoding and identification of underlying feedbacks. *Biophysical Journal*, *90*, 3120–3133.
43. Lievremont, J. P., Hill, A. M., Tran, D., Coquil, J. F., Stelly, N., & Mauger, J. P. (1996). Intracellular calcium stores and inositol 1, 4, 5-trisphosphate receptor in rat liver cells. *Biochemical Journal*, *314*, 189–197.
44. Thurley, K., Smith, I. F., Tovey, S. C., Taylor, C. W., Parker, I., & Falcke, M. (2011). Timescales of IP_3 -evoked Ca^{2+} spikes emerge from Ca^{2+} puffs only at the cellular level. *Biophysical Journal*, *101*, 2638–2644.
45. Wagner, J., Fall, C. P., Hong, F., Sims, C. E., Allbritton, N. L., Fontanilla, R. A., & Nuccitelli, R. (2004). A wave of IP_3 production accompanies the fertilization Ca^{2+} wave in the egg of the frog, *Xenopus laevis*: theoretical and experimental support. *Cell Calcium*, *35*, 433–447.
46. Handy, G., Taheri, M., White, J. A., & Borisyuk, A. (2017). Mathematical investigation of IP_3 -dependent calcium dynamics in astrocytes. *Journal of Computational Neuroscience*, *42*, 257–273.
47. Singh, N., & Adlakha, N. (2019). A mathematical model for interdependent calcium and inositol 1, 4, 5-trisphosphate in cardiac myocyte. *Network Modeling Analysis in Health Informatics and Bioinformatics*, *8*, 18.
48. Pawar, A., & Pardasani, K. R. (2022). Effects of disorders in interdependent calcium and IP_3 dynamics on nitric oxide production in a neuron cell. *The European Physical Journal - Plus*, *137*, 1–19.
49. Pawar, A., & Pardasani, K. R. (2022). Effect of disturbances in neuronal calcium and IP_3 dynamics on β -amyloid production and degradation. *Cognitive Neurodynamics*, 1–18. <https://doi.org/10.1007/s11571-022-09815-0>.
50. Pawar, A., & Pardasani, K. R. (2023). Computational model of calcium dynamics-dependent dopamine regulation and dysregulation in a dopaminergic neuron cell. *The European Physical Journal - Plus*, *138*, 30.
51. Pawar, A., & Pardasani, K. R. (2022). Simulation of disturbances in interdependent calcium and β -amyloid dynamics in the nerve cell. *The European Physical Journal - Plus*, *137*, 1–23.
52. Pawar, A., & Pardasani, K. R. (2022). Study of disorders in regulatory spatiotemporal neurodynamics of calcium and nitric oxide. *Cognitive Neurodynamics*, 1–22. <https://doi.org/10.1007/s11571-022-09902-2>.
53. Pawar, A., & Pardasani, K. R. (2023). Mechanistic insights of neuronal calcium and IP_3 signaling system regulating ATP release during ischemia in progression of Alzheimer's disease. *European Biophysics Journal*, *52*, 153–173.
54. Pawar, A., & Pardasani, K. R. (2023). Fractional order interdependent nonlinear chaotic spatiotemporal calcium and $\text{A}\beta$ dynamics in a neuron cell. *Physica Scripta*, *98*, 085206.
55. Pawar, A., & Pardasani, K. R. (2023). Fractional-order reaction-diffusion model to study the dysregulatory impacts of superdiffusion and memory on neuronal calcium and IP_3 dynamics. *The European Physical Journal - Plus*, *138*, 1–17.
56. Neher, E., & Augustine, G. J. (1992). Calcium gradients and buffers in bovine chromaffin cells. *The Journal of Physiology*, *450*, 273–301.
57. Smith, G. D. (1996). Analytical steady-state solution to the rapid buffering approximation near an open Ca^{2+} channel. *Biophysical Journal*, *71*, 3064–3072.
58. Smith, G. D., Wagner, J., & Keizer, J. (1996). Validity of the rapid buffering approximation near a point source of calcium ions. *Biophysical Journal*, *70*, 2527–2539.
59. Falcke, M. (2003). Buffers and Oscillations in Intracellular Ca^{2+} Dynamics. *Biophysical Journal*, *84*, 28–41.
60. Stern, M. D. (1992). Buffering of calcium in the vicinity of a channel pore. *Cell Calcium*, *13*, 183–192.
61. Prins, D., & Michalak, M. (2011). Organellar calcium buffers, cold spring harb. *Perspectives in Biology and Medicine*, *3*, a004069–a004069.
62. Gabso, M., Neher, E., & Spira, M. E. (1997). Low Mobility of the Ca^{2+} buffers in axons of cultured aplasia neurons. *Neuron*, *18*, 473–481.
63. Lopez-Caamal, F., Oyarzun, D. A., Middleton, R. H., & Garcia, M. R. (2014). Spatial quantification of cytosolic Ca^{2+} Accumulation in non-excitable cells: An analytical study. *IEEE/ACM Transactions on Computational Biology and Bioinformatics*, *11*, 592–603.

64. Wacquier, B., Combettes, L., Van Nhieu, G. T., & Dupont, G. (2016). Interplay between intracellular Ca^{2+} oscillations and Ca^{2+} -stimulated mitochondrial metabolism. *Scientific Reports*, *6*, 1–16.
65. Stamatakis, M., & Mantzaris, N. V. (2006). Modeling of ATP-mediated signal transduction and wave propagation in astrocytic cellular networks. *Journal of Theoretical Biology*, *241*, 649–668.
66. Han, J. M., & Periwal, V. (2019). A mathematical model of calcium dynamics: Obesity and mitochondria-associated ER membranes. *PLoS Computational Biology*, *15*, e1006661.
67. Arruda, A. P., Pers, B. M., Parlakgul, G., Guney, E., Inouye, K., & Hotamisligil, G. S. (2014). Chronic enrichment of hepatic endoplasmic reticulum-mitochondria contact leads to mitochondrial dysfunction in obesity. *Nature Medicine*, *20*, 1427–1435.
68. Montalto, D. (2021). Focus on obesity. *OBG Management*, *33*, <https://doi.org/10.12788/obgm.0095>.
69. Pi-Sunyer, F. X. (2002). The medical risks of obesity. *Obesity Surgery*, *12*, S6–S11.
70. Gilibert, J. A. (2001). Energized mitochondria increase the dynamic range over which inositol 1,4,5-trisphosphate activates store-operated calcium influx. *The EMBO Journal*, *20*, 2672–2679.

Publisher's note Springer Nature remains neutral with regard to jurisdictional claims in published maps and institutional affiliations.

Springer Nature or its licensor (e.g. a society or other partner) holds exclusive rights to this article under a publishing agreement with the author(s) or other rightsholder(s); author self-archiving of the accepted manuscript version of this article is solely governed by the terms of such publishing agreement and applicable law.